We are IntechOpen,
the world's leading publisher of
Open Access books
Built by scientists, for scientists

6,900
Open access books available

186,000
International authors and editors

200M
Downloads

Our authors are among the

154
Countries delivered to

TOP 1%
most cited scientists

12.2%
Contributors from top 500 universities

CLARIVATE ANALYTICS
BOOK CITATION INDEX
INDEXED

WEB OF SCIENCE™

Selection of our books indexed in the Book Citation Index
in Web of Science™ Core Collection (BKCI)

Interested in publishing with us?
Contact book.department@intechopen.com

Numbers displayed above are based on latest data collected.
For more information visit www.intechopen.com

Monte Carlo Simulations of Microchannel Plate–Based, Time-Gated X-ray Imagers

Craig A. Kruschwitz and Ming Wu
National Security Technologies, LLC
USA

1. Introduction

In the last two decades, high-speed, time-gated Microchannel plate (MCP) x-ray detectors have proven to be powerful diagnostic tools for two-dimensional, time-resolved imaging and time-resolved x-ray spectroscopy in the field of laser-driven inertial confinement fusion and fast Z-pinch experiments (McCarville et al., 2005; Oertel et al., 2006; Bailey et al., 2004). These detectors' quantitative measurements are critical for a comprehensive understanding of the experimental results. To assist their characterizations and to aid design improvements, a more comprehensive Monte Carlo simulation model for the MCP detector is needed.

The MCP detectors are widely used as electron, ion, and x-ray detectors, as well as imaging tools in many areas of scientific research. Their principles of operation have been documented in the literature (Wiza, 1979; Fraser et al., 1982; Fraser et al., 1984; Kilkenny, 1991) as have extensive research efforts to characterize detection sensitivity (Ze et al., 1999; Landen et al., 1993; Landen et al., 1994), angular and energy dependences (Hirata et al., 1992; Landen et al., 2001; Rochau et al., 2006), and temporal and spatial resolution (Robey et al., 1997). In many previous studies, a discrete dynode gain model was used to describe the MCP gain dependence on the applied voltage (Eberhardt, 1979). This dependence is extremely nonlinear. The discrete dynode model assumes that the MCP can be treated as a conventional, discrete-stage electron multiplier with a fixed number of stages. This gain model uses a few free parameters, chosen to best fit a certain MCP's data. The discrete dynode model seems to work well to describe the behavior of MCPs under some circumstances, but several factors are not included when inferring the secondary electron yield from gain measurements. For example, the discrete dynode model assumes that the number of dynode stages is independent of the applied voltage on the MCP (the number of stages is chosen to best fit the gain vs. voltage data), which is unlikely to be valid.

In addition to the discrete dynode model, previous researchers have also performed Monte Carlo–based computer simulations of the MCP response to a steady-state voltage for straight and tilted microchannels (Guest, 1971; Ito et al., 1984; Choi & Kim, 2000; Price & Fraser, 2001). These simulations apparently did not include the constraint of energy conservation for the secondary electrons. This constraint prevents the aggregate energy of the emitted electrons from exceeding the primary electron energy. Furthermore, these previous efforts omit the effects of low-energy electrons' elastic scattering from the channel walls, potentially an important effect for the low-impact energies prevalent in an MCP electron cascade. A further difficulty encountered by all such previous efforts (and, indeed,

the present one) is that a fair number of adjustable parameters in these simulations cannot be unambiguously determined from the existing data. Consequently, inconsistent parameter sets appear in the literature, with some more robustly constrained by the data than others.

This chapter is divided into several parts. To begin we present a somewhat detailed description of our simulation model, which builds upon our earlier work (Wu et al., 2008; Kruschwitz et al., 2008). Section 2 lays out the secondary emission equations used in the simulations and briefly describes how we approximate MCP saturation. Results from various sets of simulations of MCPs under both steady state and pulsed bias voltages are shown. Comparisons of simulated and measured MCP gain in DC mode appear in Section 3. MCP performance under an ideal square waveform pulse is described in Section 4. An example of how to use Monte Carlo simulation to optimize MCP detector design is shown in Section 5, and is followed by a detailed comparison of the simulations with experimental results in pulsed mode to better evaluate the effectiveness of the model. Comparisons between experimental and simulation results of detector optical gate profile and sensitivity uniformity, as well as detector gain under pulsed operation are discussed in Sections 6 and 7. MCP saturation in DC and pulsed modes is addressed in Section 8. Spatial resolution of the MCP detector is discussed in Section 9. We conclude with some simulations of small-pore (2 µm) MCPs, making some predictions about their potential performance in x-ray imaging systems in Section 10

2. Model and computational algorithm

An MCP is essentially an array of parallel continuous electron multipliers. A schematic of an MCP x-ray detector is shown in Fig. 1.
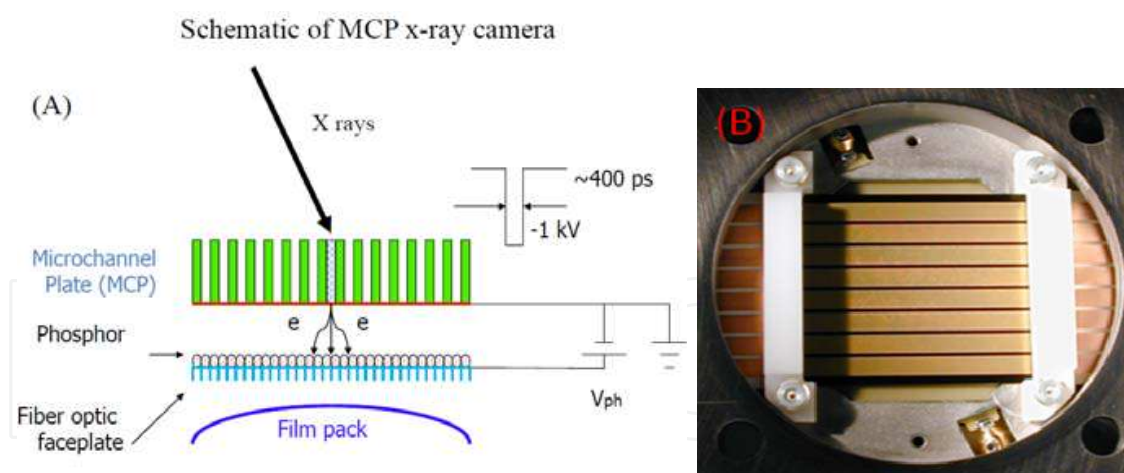

Fig. 1. (A) Schematic of a high speed time-gated MCP based x-ray detector. The MCP is usually biased by a negative voltage while the phosphor is biased by a positive voltage. (B) Eight-strip MCP detector (NSTec H-CA-65).

For our work the individual MCP channels were typically ~10 µm in diameter, with a 12 µm spacing between pore centers (denoted D_{cc} throughout), and with a plate thickness of 450–600 µm; recently, small-pore MCPs with pore diameters as small as 2 microns (D_{cc} = 3 µm) have become available, and these are studied here as well. Generally, the channels are set at an angle, α, relative to the MCP surface normal, called the bias angle. The MCP is also characterized by the ratio of its thickness to the channel diameter, or its L/D ratio.

We assume that MCP electron cascade dynamics can be approximated by the behavior of a single microchannel. For our purposes, it is acceptable to assume that all microchannels in a particular plate are identical because we are neglecting any cross-talk effects between adjacent channels. Note, however, that previous researchers have reported that when the MCP is operated at high count rates or used for hard x-ray detection, effects between neighbouring channels may occur (Fraser et al., 1993; Shikhaliev, 1997). Also, pore-bleaching effects, where the fields generated in a pore affect the gain in adjacent pores, are not used in these simulations; they are assumed to be negligible in subnanosecond MCP gating for the detection of soft x-rays, which is our focus.

The cascade is taken to be initiated by some number of incident electrons. The actual number of primary electrons is sampled from a Poisson distribution. The primary electrons are assumed to be generated by interactions of x rays or UV photons with the reduced lead glass channel surface. The directions in which the primary electrons are emitted are given by a pair of angles for each electron. The first of these angles is defined relative to the surface normal and is assumed to obey a cosine probability distribution:

$$P(\theta) \propto \cos(\theta) \tag{1}$$

where θ is the angle relative to the surface normal. The second angle is an azimuthal angle sampled from a uniform distribution between 0 and 2π. The initial energies of the primary electrons are somewhat more difficult to determine and are expected to be different for x-ray and UV sources. For x rays, we presume the energies (E_s) are sampled from the following probability distribution (Scholtz et al., 1996):

$$f(E_s) = C \cdot \exp\left\{ -\frac{\left[\ln(E_s / E_0)\right]^2}{2\sigma^2} \right\} \tag{2}$$

where $E_0 = 2.3$ eV, the most probable energy, $\sigma = 0.65$, and C is a normalization constant. The same probability distribution is used to determine the initial energies of the secondary electrons. We use this distribution in lieu of measurements of the energy distribution of electrons produced from the interaction of keV x rays with the MCP glass. The values for E_0 and σ approximately match the experimental data of Authinarayanan & Dudding (1976) on MCP glass secondary electron emission.

For UV photons, the initial energies of the primary electrons are determined by the work function of the reduced lead glass material of the MCP and the UV photon energy, the value of the photon energy being 6.2 eV in our experiments. The work function of the reduced lead glass is poorly known, but values of around 5 eV have been quoted in the literature (Melamid, 1972). Therefore, we deduce that photoelectrons produced by the UV photons have an initial energy of ~0.1–1.2 eV. Simulation results with primary electron energies in this range match our data quite well.

In this model, we assume that only the photoelectrons and Auger electrons generated adjacent to the microchannel can initiate a cascade within the channel, in agreement with experimental observation for <5 keV x rays (Rochau et al., 2006). The initial photoelectrons are generated in a timeframe ($<10^{-12}$ s) that is much shorter than the transit time of the cascading electrons. The time lag of secondary emission is estimated to be 10^{-13} to 10^{-14} s, much shorter than any timescale relevant to electron-cloud effects. Thus, we suppose that

secondary electrons are generated instantaneously when a primary electron hits the lead glass surface. For the simulations presented in this chapter, all electron cascades begin at the MCP input face. For each electron incident on the channel wall, equations dependent on the incident energy and angle are used to determine the mean secondary emission yield.

The actual value of the average secondary emission yield for a primary electron incident on the MCP channel surface at angle θ_i and with energy V_i is determined by (Vaughan, 1989)

$$\delta\,(V_i, \theta_i) = \delta_m(\theta_i) \left(\frac{V_i}{V_m(\theta_i)} \exp\left[1 - \frac{V_i}{V_m(\theta_i)} \right] \right)^s \tag{3}$$

where s is a free parameter whose value is chosen to best fit the data (we use $s = 0.62$), and $V_m(\theta_i)$ and $\delta_m(\theta_i)$ are given by the following equations (Vaughan, 1989):

$$V_m(\theta_i) = V_m(0)\left(1 + k\frac{\theta^2}{2\pi} \right) \tag{4}$$

$$\delta_m(\theta_i) = \delta_m(0)\left(1 + k\frac{\theta^2}{2\pi} \right) \tag{5}$$

where $V_m(0)$ is the impact energy yielding the maximum mean secondary electron yield $\delta_m(0)$, at normal incidence, and k, a constant determined by the data (between 0 and 2), is usually a surface smoothness indicator. Values between 0.5 and 1 fit our data well. We take $V_m(0)$ to be ~300 eV and $\delta_m(0)$ to be 3–4, as in the experimental results of Authinarayanan & Dudding (1976). Final values are chosen to match our measurements of the MCP sensitivity versus static bias voltage. The actual secondary yield is determined by random sampling of a Poisson distribution with a mean value of $\delta(V_i, \theta_i)$, determined using Eq. (3).

Other authors (Guest, 1971; Ito et al., 1984; Choi & Kim, 2000; Price & Fraser, 2001) have used a variety of alternate forms for Eqs. (3)–(5), each with their own adjustable parameters. The manners in which these models simulate the secondary emission processes in an MCP are very similar. This is largely because the majority of electron-channel wall collisions are low energy (<50 eV) a domain in which each of these models is nearly linear and for which there is little measured data. Furthermore, measurements of the dependence of secondary emission on the incident angle of the primary are typically at angles between zero degrees (normal incidence) and 60–70 degrees. In the channel, however, even for low bias voltages, most primaries impact at a near grazing angle (~70–80 degrees), where there is essentially no data. Thus, the published models are little more than useful starting points for modelling secondary emission in the MCP.

Knowing the number of secondary electrons, each electron's initial energy is assigned by sampling Eq. (2). Note that various forms for the secondary energy distribution have been used by different authors (Guest, 1971; Ito et al., 1984; Choi & Kim, 2000; Price & Fraser, 2001). We have found that the specific form of the distribution generally has little effect on the simulation results. Of greatest importance to the outcome is the value of the most probable energy. While we assume the emission energies of the secondary electrons to be uncorrelated, we do require that energy is conserved by ensuring that the sum of the secondary electron emission energies be less than the impact energy of the primary electron. As it happens, a straightforward sampling of Eq. (2) only very rarely violates the

conservation condition, thus we implement energy conservation by repeatedly sampling the secondary electron energies from Eq. (2) until the conservation condition is met.

The direction in which each secondary electron is emitted is sampled from a cosine distribution (Eq. (1)). We assume that the secondary electrons' emission angles are fully uncorrelated, independent of the incident energy and angle, and uncorrelated with the emission energies. Experiments show these to be reasonable conclusions (Bruining, 1954). The trajectories of the secondary electrons are then calculated using nonrelativistic equations of motion. Because the maximum electron kinetic energies are ≤1 keV, the problem can safely be treated nonrelativistically. After the electron equations of motion are solved, the electron's impact energy and angle with the channel wall are determined, giving the initial conditions for the next generation of electrons. This process repeats until the electrons emerge from the output channel end or the cascade dies out, yielding no output electrons. The positions and velocities at the output of the channel are determined for those electrons that emerge from the channel. Finally, these electrons are then accelerated by the voltage, V_{ph}, applied between the MCP output face and the phosphor to determine their final positions at the phosphor. In our model electron scattering from the phosphor has not been taken into account.

In previous Monte Carlo simulations (Guest, 1971; Ito et al., 1984; Choi & Kim, 2000; Price & Fraser, 2001), the possibility of the incoming electrons' elastic reflection was neglected. The effect was first considered in our previous work (Wu et al., 2008), and we continue to include the effect. In our simulations elastic scattering was an important effect, particularly for low-bias voltages. It was necessary to include elastic scattering in order to use one parameter set to describe the MCP gain variation with bias voltage over the full range of bias voltages of interest. The probability of electron reflections from lead glass at normal incidence as a function of energy was studied by Scholtz et al. (1996). They discovered that for 10 eV primary electrons incident normal to a lead glass surface, the majority of the resulting secondary electrons were elastically reflected primary electrons, decreasing to just a few percent for 100 eV primary electrons. Unfortunately, the research did not examine any angular dependence for this effect, and neither, to our knowledge, has subsequent research (Cimino et al., 2004). Nevertheless, we admit the possibility of elastic reflection of incident electrons. We use the following equation to describe the probability with which an electron with energy V_i is elastically reflected from the channel wall (Cimino et al., 2004):

$$\delta_{el} = \frac{\left(\sqrt{V_i + V_0} - \sqrt{V_i}\right)^2}{\left(\sqrt{V_i + V_0} + \sqrt{V_i}\right)^2} \qquad (6)$$

where V_0 is an unknown parameter chosen to best fit the data. We find that a value ~165–175 eV fits our data well. Eq. (6) is sampled to determine the probability that an electron is elastically reflected after a collision with the channel wall. If reflection occurs, then the axial and angular components of the electrons' velocity are left unchanged, while the radial component is reversed. If reflection does not occur, the secondary electron yield and initial properties of the secondary electrons are determined, as described above.

Channel gain saturation, arising from the presence of large numbers of electrons in the channel, and the build-up of positive wall charge is also included in the model. The effect of the electrons in the pore is approximated by estimating the electrostatic potential due to the electrons cascading in the pore. The MCP channel is divided into some number of axial

segments. In general, we take the segments to be on the order of the average axial distance travelled by the electrons before impacting the channel wall. For a D = 10 μm pore MCP this distance is ~10 μm. The cloud of electrons in each segment can be approximated as a disc of negative charge, and the electrostatic potential calculated accordingly. The effect of this potential is twofold. First, radial fields exert a force on secondary electrons emerging from the channel wall. When the number of electrons in the channel is high, the exerted force can shorten the electrons' time of flight, thus reducing the time that the axial field accelerates the secondary electrons. The electrons therefore impact with less energy, reducing the average secondary electron yield from the collision. The electron density distribution is constantly changing such that a precise calculation is too complex to be tractable; therefore, the effect for each generation of new secondary electrons is approximated. The second effect that arises is due to axial fields that act as perturbations to the applied accelerating voltage. Generally, these perturbations reduce the accelerating field's strength. This, in turn, reduces the average secondary yield.

As electrons are pulled from the channel walls, a net positive charge remains. The time scale over which the extracted charge is replenished by the current flowing through the MCP is on the order of milliseconds because the lead glass is essentially an insulator. This time scale is much longer than either the ~180–220 ps electron transit time or the subnanosecond gating voltage pulse duration, and so is unimportant for our simulations. The effects of the build-up of positive charge in the channel wall (or wall charging) are similar to those of space charge. Radial fields affect the time of flight of secondary electrons that are emitted into the channel in a way that reduces the gain of subsequent generations. Also, the axial fields perturb the applied fields, thereby altering the trajectories of the electrons so that the gain of secondary electrons diminishes. Furthermore, because the wall charge is neutralized over such long time scales, its build-up can affect subsequent cascades in a given channel, should any occur, and thus has consequences for the linearity of the detector over long exposures, i.e., of order nanoseconds or microseconds. In the work presented here, we are only concerned with a single cascade in a given channel.

Our model simulates MCP response to both static and pulsed voltage biases. Because the value of the voltage does not change over the duration of the electron cascade, static voltage bias is easily understood. We assume, following the work of Gatti et al. (1983), that the electric field is parallel to the channel axis for static voltages rather than perpendicular to the MCP face. According to Gatti et al. (1983), the axial field direction results from the azimuthal current flow around the channel wall's diameter. This current flow ultimately rotates the electric field from a near-perpendicular orientation when the voltage is first applied to an orientation parallel to the channel axis after some milliseconds. In contrast to static bias voltages, for simulations using subnanosecond pulsed voltages, the field is taken to be perpendicular to the face of the MCP.

Time-dependence of the voltage pulse is approximated within the simulation as follows: when a secondary electron is created, the value of the voltage at the time of creation (understood to be the same as the time of the collision of the parent electron with the channel wall) is determined and the electron's trajectory is calculated using that voltage. This approximation should be reasonable if the time scale over which the voltage changes is less than the 5 to 10 ps time of flight of a typical electron in the channel. This assumption holds for the voltage pulses we investigate in this chapter.

The effects of pore end spoiling, where the thin metal layers coated onto the MCP penetrate a small distance into the pore (typically 1–1.5 pore diameters), are also approximated in the

model by setting the field to zero in this region for static and pulsed bias. The zero-field approximation agrees with the work of Price & Fraser (2001), who performed two-dimensional electric field calculations for a single channel's end-spoiled region, showing that the field is close to zero in the end-spoiled region. Landen et al. (2001) show that at high-voltage biases fringing fields in the end-spoiled region may be significant enough that the zero voltage approximation may cease to be valid, and cite experimental results suggesting this is the case. However, the effect primarily occurs when the flux of x rays or UV photons are at a steep angle of incidence relative to the MCP surface. Because the UV and x-ray sources were normal to the MCP surface in the experiments we will later describe, we retain the zero-field approximation in the end-spoiled region.

This completes our description of the Monte Carlo simulation model. The remainder of this chapter discusses simulation results and compares them to experimental data.

3. MCP sensitivity under DC voltage bias

Although these simulations can be adapted to MCPs with almost any geometry, we have concentrated most of our modelling efforts on an MCP with a 10 μm channel diameter and a thickness of 0.46 mm (L/D = 46). The simulation parameters are discussed in Section 2. A large amount of experimental data exists for these types of MCPs and can be used for comparison. Fig. 2 shows simulation results for an MCP with a steady-state bias of –1000 V. The simulation was initiated by introducing five electrons near the MCP input end. The gain histogram for 2000 separate runs shows that the average gain is about 3×10^4, but a considerable spread in the gain clearly exists. This is a consequence of the statistical nature of the secondary emission process. There is a clear indication of a peak in the gain histogram near 15,000. The transit time distribution for these runs looks essentially Gaussian, with a mean transit time of 188 ps and a full-width half-maximum (FWHM) transit-time spread (TTS) of 53 ps. We lack transit-time measurements for the MCPs we are simulating (such measurements are difficult to make), but these transit times are consistent with existing measurements (Ito et al., 1984).
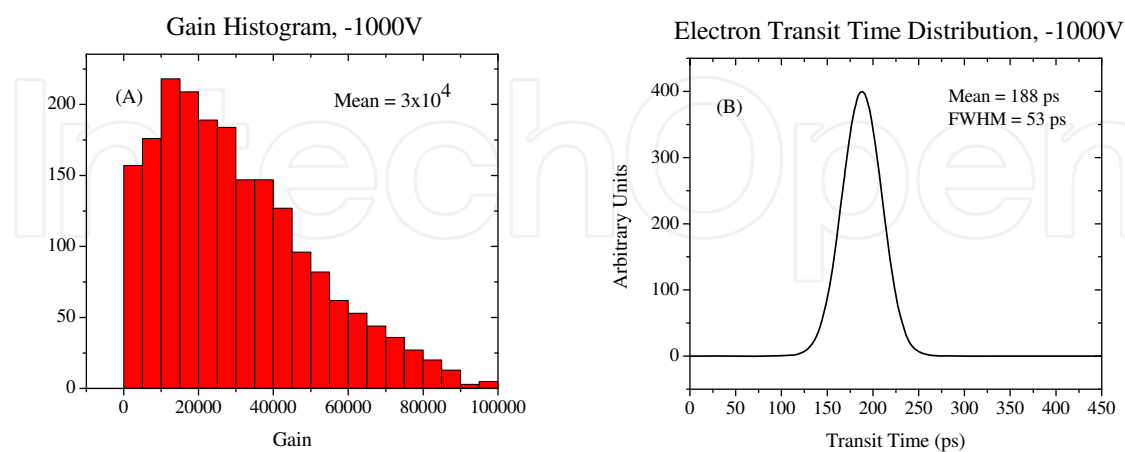

Fig. 2. Simulation results for an L/D = 46, 10 μm pore diameter MCP biased at- 1000 V DC. (A) Gain histogram; (B) electron transit-time distribution.

Fig. 3 shows simulation results for an identical MCP, but with an applied voltage bias of –600 V DC. The average gain is 121, more than two orders of magnitude lower than for the

–1000 V DC simulations, and the gain histogram lacks any indication of a peak. The lower gain, the result of smaller electron impact energies, results in smaller secondary electron yields. The mean transit time is 219 ps, ~30 ps longer than for the –1000 V DC simulations. This is a consequence of the decreased acceleration in the –600 V DC bias case. The electrons travel a shorter distance down the channel between collisions, and thus, require more time to reach the output end. Also, the TTS for the –600 V case is 73 ps, much longer than the –1000 V DC case, primarily because the spread in secondary electron energy and direction play a greater role at lower bias voltages where the electrons travel shorter distances between collisions and impact the channel wall with lower energy.
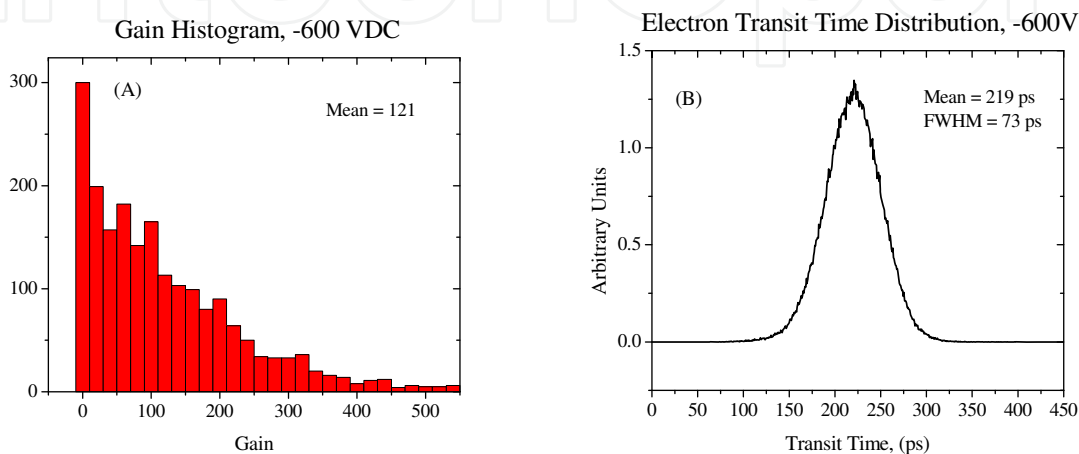
Fig. 3. Simulation results for an L/D = 46, 10 µm pore diameter MCP biased at -600 V DC. (A) Gain histogram; (B) electron transit-time distribution.

In order to check the validity of our simulation results, we compared the modelled versus measured MCP sensitivities. The experimental details of the MCP DC sensitivity measurements using a Manson x-ray source were described previously (Wu et al., 2008). The detector consists of an MCP coated with six separate strips (each 4 mm wide × 40 mm long, separated by 2 mm) on the input (bias) and output (ground) surfaces, a P43 phosphor screen coated on a fiber-optic faceplate at positive potential and a coherent fiber bundle coupled between the faceplate and a charge-coupled device (CCD). A negative-bias voltage was applied to each strip, and the phosphor-coated fiber-optic faceplate was held at +3000 V with respect to the MCP back surface. The Manson source was operated at 8 kV with 0.3 mA of emission current using aluminium anodes that have emission peaks at about 1.5 keV. The x-ray flux and spectrum was monitored by an Amptek XR-100-CZT x-ray pulse-height spectrometer. The MCP were placed ~2.7 m from the Manson source to obtain a uniform x-ray flux on all strips. Two Uniblitz x-ray shutters installed on each line of sight ensured equal x-ray exposures. Beryllium filters were used on both lines of sight to block light emission from the filament. Relative sensitivities were measured as a function of voltage for potentials ranging from -450 to -950 V, incremented by 50 V. Three images were taken at each voltage setting. The measured intensity was obtained by averaging all six strips and the error bar was given by one standard deviation of sensitivity over the entire MCP.

Both modelled and measured sensitivities are plotted versus voltage in Fig. 4. The simulated gains have been scaled so that the model value at -450 V is set to the average of the measured data. Clearly the model reproduces the trend in the measured data extremely well over virtually the entire voltage range. However, the data show some levelling off at -950 V,

which is not seen in the simulations. This levelling off is due to the onset of saturation in the CCD used to collect the data, and is not an effect of the MCP. This excellent agreement between the experiment and simulation indicates that the parameters used in the model as described in Section 2 are reasonable. With the success in DC simulation, it gives us confidence to attempt pulsed mode simulations.
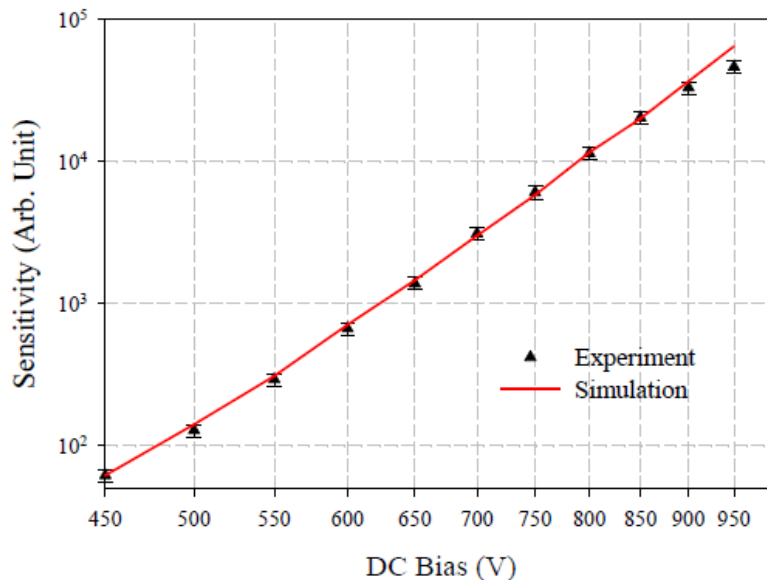

Fig. 4. Comparison of simulated and measured MCP relative sensitivity vs. DC voltage shows that parameters used in our model agree with existing experimental data.

4. MCP performance under an ideal square waveform

Initially, our investigation of pulsed MCP response using our Monte Carlo simulation model was conducted by looking at an ideal square-wave voltage pulse. The ideal square-wave, though only an approximation of a real voltage waveform, offers useful insights about expected MCP behavior under voltage pulses of varying widths and peaks. The simulations used a –700 V pulse and a DC offset varied from +400 V to –500 V in increments of 50 V so that the peak voltage varied from –300 to –1200 V. The pulse widths were varied from 50 to 300 ps in 50 ps increments. Five primary electrons initiated the cascades.

The peak MCP gain as a function of peak voltage plotted on a log-log scale is shown in Fig. 5. A few observations can be made about these results. First, it is apparent that for pulse widths shorter than the ~200 ps transit time, there is essentially no gain for a reverse DC bias. This is unsurprising, since very few electrons make it through the MCP in such a short time, and the direction of the DC field acts to prevent any electrons emerging from the output end once the pulse has stopped. Second, it is evident that the relative gain as a function of peak voltage varies greatly for different voltage pulse widths. For pulse widths <250 ps there is a larger gain exponent (n in the expression $G \sim V^n$) as a function of peak voltage than there is for 250 and 300 ps pulses, which give a gain exponent of $n = 10.8$, close to the $n = 11$ DC mode gain exponent. Since these are ideal square waveforms, it is expected that the sensitivity of gain to peak applied pulsed voltage should be nearly identical to the DC results when the pulse length is longer than the electron transit time, as the MCP is

essentially operating in DC mode for such pulses. The primary difference between the longer pulses and DC mode operation is the slightly different electric field configuration referred to in Section 2. However, the gain behavior of the MCP departs substantially from the DC mode when the pulse width is smaller than the transit time of electrons. The shorter the pulse width the stronger the deviation from the DC mode will be, as shown in Fig. 5. It is evident that when the applied voltage pulse width becomes shorter than the transit-time, it is no longer possible to obtain the full gain from the MCP during the pulse. In this case, the gain of detector has a higher order of nonlinearity than in DC mode.
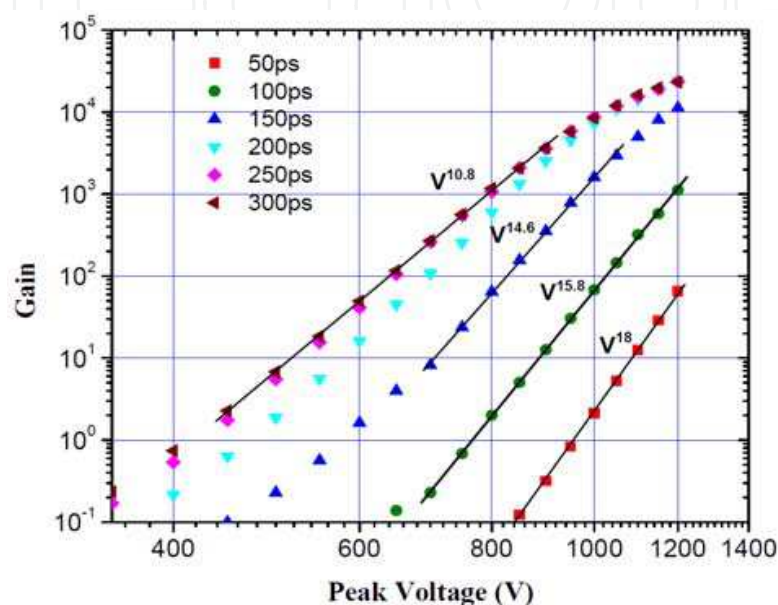
Fig. 5. Simulated peak gain vs. peak voltage for an ideal square wave. The result indicates that shorter pulse widths deviate most strongly from DC mode.

The increase in the gain exponent for pulses shorter than the transit time has previously been reported by Landen et al. (1993), who described data giving a gain exponent of $n = 20$ for voltage pulses shorter than the transit time of the electron cascade through a similar ($L/D = 46$) MCP. From our simulations, a gain exponent of $n = 18$ is estimated for the 50 ps ideal square pulse, somewhat smaller than they report. It is difficult to make a direct comparison between the Landen et al. (1993) results and these simulations because they made no measurements of the actual voltage waveforms on the MCP. Thus, the precise time dependence of the voltage pulses is unknown.

These simulation results suggest a limitation to how fast one can gate the MCP. For a particular MCP, when the width of the applied voltage waveform is less than the average transit time, the detector's gain will be reduced significantly. A gain reduction of more than three order of magnitude is calculated when the pulse width is reduced from 250 to 50 ps with a peak voltage at 1000 V. This is not a surprising result: a shorter voltage pulse means fewer electrons transit the MCP and fewer collisions with enough energy to produce secondary electrons occur. However, it offers further illustration of the difficulty of gating an MCP with pulses comparable to and shorter than the transit time. The maximum voltage that could be applied to the $L/D = 46$, 10 µm pore MCP is most likely limited to be about -1200 V to avoid breakdown. The MCP's gain would be <100 for a 50 ps square pulse with a -1200 V peak voltage. As described above, for pulse widths shorter than the transit time the

MCP exhibits a larger gain exponent. Therefore, for such voltage pulses the relative detection sensitivity of the MCP follows a higher power law. In other words the MCP is much more sensitive to peak voltage. Thus, slight variations in the peak voltage along the MCP, which can result from attenuation of the voltage pulse along the MCP strip and reflections from the strip ends, will have a much greater impact on the detection uniformity along the MCP strip for pulse widths shorter than the transit time.

5. MCP performance optimization in pulsed mode

The Monte Carlo simulation code can also be used to predict detector performance, providing guidelines for selecting detector operating parameters. An L/D = 46 MCP is used here as an example of how to employ our Monte Carlo approach to achieve a narrow optical gate profile without significantly reducing detection sensitivity. The CPS3 pulser system from Kentech Instruments Ltd. is widely used in the high-energy density physics (HEDP) community to drive gated MCP detectors. Using a measured waveform from a CPS3 pulser and a 300 ps near-square-top pulse-forming network (PFN), we cut 50 ps increments from the 'flat' section of the waveform, thereby constructing hypothetical waveforms for use in the simulation code with flat tops of 300, 250, 200, 150, 100, 50, and 0 ps. The flat-top pulse width for the input waveforms here is defined as the width of 95% of peak voltage, while the 0 ps flat-top waveform is simply a combination of the rising and falling edges of the measured pulse. The peak voltage of the waveforms was scaled to be near 800 V; DC transit times at 800 V are near 200 ps. Seven of the input waveforms and simulated MCP gate profiles are shown in Figs. 6(A) and (B). Significant changes in the FWHM of the gate profiles and the MCP relative gain are observed. The FWHM of the gate profiles vs. the pulse width of the flat top is shown in Fig. 7(A). Gate profile FWHMs are 230, 186, 150, 115, 105, 99, and 97 ps, respectively, for the 300, 250, 200, 150, 100, 50, and 0 ps flat-top waveforms. Of note is that the limiting temporal resolution, as defined by the gate profile FWHM, for the L/D = 46, 10-micron pore MCP appears to be about 100 ps regardless of the voltage pulse width.
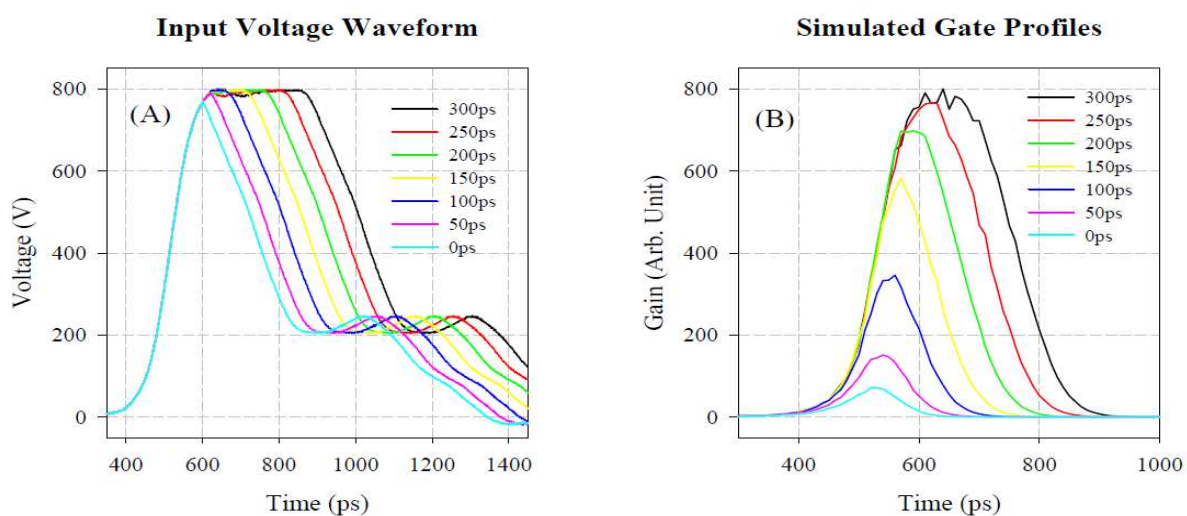

Fig. 6. (A)Input voltage waveforms and (B) Simulated optical gate profiles for 10 μm and L/D = 46 MCP.

The integrated gate profiles and relative peaks of the gate profiles with these voltage waveforms are shown in Fig. 7(B). The results show that the overall detection sensitivity, defined as the integrated gate profile, will be reduced by about 60% when the flat top of waveform is reduced from 300 to 150 ps, while the gate profile peak amplitude changes only about 25%. The overall detection sensitivity will be reduced by about a factor of ten when a 50 ps flat-top waveform is applied as compared with the 300 ps flat-top waveform. Depending on specific experimental requirements, a compromise between the detection sensitivity and temporal resolution is necessary. These results indicate that when the 150 ps flat-top waveform is selected, the predicted gate profile width, 120 ps FWHM, is close to the shortest achievable gate profile. At the same time, with only a 25% reduction in the peak gain, relatively little is sacrificed in the way of detector sensitivity. Thus the 150 ps flat-top PFN would seem to offer a reasonable compromise. In the following section we discuss measurements made using a 150 ps flat-top PFN and comparisons to further simulations.
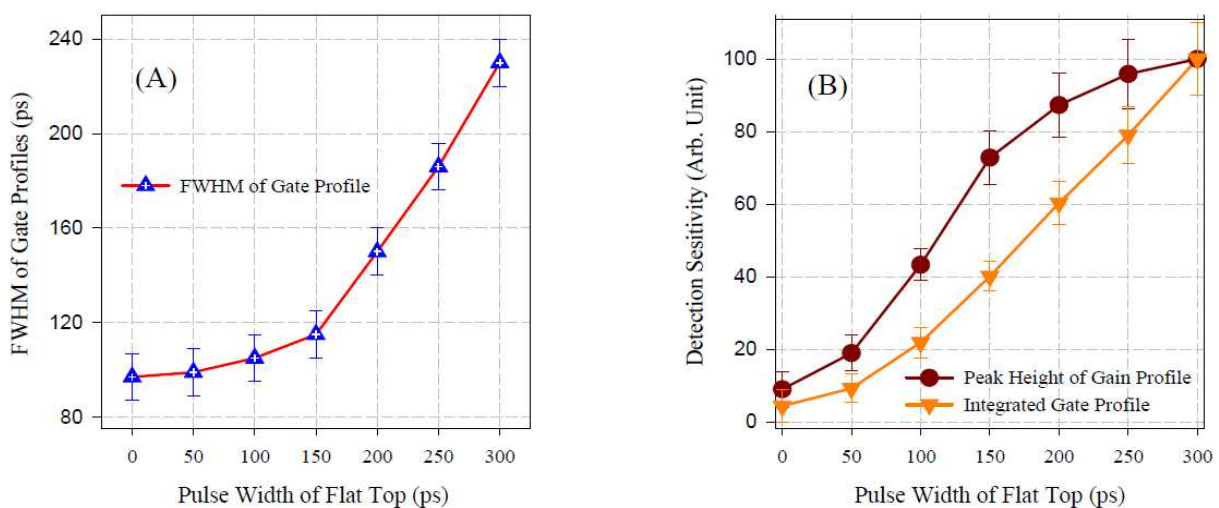
Fig. 7. (A) Variation of FWHM of the simulated gate profiles versus waveform flat-top width; (B) detection sensitivity versus waveform flat-top width.

6. Optical gate profiles and detector uniformity

Optical gate profiles and detector uniformity along the MCP strip are two important parameters for HEDP diagnostics applications. The ability to use simulations to predict the performance of a time-gated MCP detector is highly desired in the HEDP community, because of the time and high cost involved in characterizing detector performance experimentally. Because the detector gain with applied voltage in pulsed mode is highly nonlinear, slight variations in the voltage waveform on the MCP strips can significantly change their performance. The actual voltage waveform on each MCP strip on each detector can be affected by assembly processes and component quality, even for detectors of the same design. For high quality measurements, it is necessary to characterize the performance of each individual detector. Once we are able to verify our Monte Carlo code and the MCP physical model by comparison to experiment, the simulation code can be used to predict the performance of the MCP detectors when actual waveforms on the MCP strips are precisely measured.

Experimental details of the characterization process have been published before (Kruschwitz et al., 2008; Rochau et al., 2008) and will only be described briefly here. MCP detector characterizations were conducted at the Short-Pulse Laser Facility at National Security Technologies, LLC, which provided 200 nm laser light with a 150–200 fs pulse width at 150–200 μJ energy per pulse. The laser beam was expanded to cover the entire MCP detector, and uniformity of the laser beam was achieved using a homogenizer and diffuser. The laser flux was adjusted with neutral density filters to ensure that the MCP was not saturated. A coherent fiber plug was used to couple the phosphor and the CCD camera.

The detector used in the experiment is the NSTec H-CA-65 camera shown in Fig. 1, an eight-frame, gated MCP framing camera that uses a rectangular MCP 42 × 48 mm in size with a 38 × 42 mm active area. The MCP is rimless, has 10 μm diameter pores, a pore length of 460 μm, and an open area ratio of 65%. Eight independent 4 mm wide striplines, comprised of 5000 Å of Cu with an overcoat of 1000 Å Au, are coated onto the MCP with an impedances of ~19 Ω. The internal circuitry consists of input and output flexible circuit boards. The input circuit board has 20 Ω transmission lines, while the output circuit board has 20 to 50 Ω transmission line tapers to prevent any reflections of the input high-voltage (HV) pulse. The MCP is gated using a pulse from a Kentech CPS3 pulser and a PFN that provides an approximately 150 ps flat-top (450 ps FWHM) voltage pulse with a peak amplitude of approximately −1500 V at the input of the detector. Impedance mismatches at the detector input reduce the peak voltage on the MCP to approximately half of that value because only about -800V pulse waveform is needed to meet our experimental conditions.

Experimental optical gate profiles were obtained using the following procedure. MCP detector images were recorded for a series of time delays between the laser and the HV pulse on the MCP. The timing of the laser was measured by a fast photo-conductive diode (PCD), while the timing of HV pulse was given by the CPS3 output monitor. Five images were taken at each time delay. The time delays are determined from the relative timing between the PCD signal and the voltage pulse as measured on a 16 GHz, 50 GS/s oscilloscope. The 50% points of the rising edges on each of these signals could be determined to <10 ps. The timing jitter in the experiments was about ≤50 ps. The gain at a specific time and location on the MCP striplines is determined using the following procedure: (1) Subtract the CCD background from the image; (2) Divide the background subtracted image by the flat-field of the beam profile taken with an applied DC voltage; (3) Integrate a narrow region around the spatial location of interest to get the average intensity; (4) Divide the average intensity by the measured laser energy. (5) The gate profiles are obtained by sorting the averaged intensities of locations of interest by the measured time delays with a bin width of 10 ps. The position-dependent gate profiles along the MCP strip are given in Fig. 8 (B).

Due to the non-linearity of gain with applied voltage, it is critical to precisely measure the voltage waveforms on the MCP strip in order to make a meaningful comparison between the simulations and experiments. The details of the experimental setup and procedure for making these measurements have been described previously (Rochau et al., 2008) and will only be summarized here. A high-impedance GGB Industries Model-35 Picoprobe is used to measure the time dependent voltage waveform at various spots along an MCP stripline. The probe has a 20 μm tungsten wire tip, an input impedance of 1.25 MΩ, and a frequency response from DC to 26 GHz. The probe is mounted on an x-y-z station controlled by step motors, so it can move to any desired location on the strip with high accuracy. The voltage

waveforms at different positions along a particular MCP strip, as measured with the Picoprobe, are shown in Fig. 8(A). The input voltage waveform for the detector is a near-square waveform, but the waveform on the MCP strip is quite different, with essentially no flat top visible. Also, transmission loss on the strip can be significant and can cause the voltage waveform to vary along the strip. The amplitude of the voltage pulse at the strip's center is less than at beginning of the strip due to attenuation of the voltage pulse along the MCP strip. However, the voltage pulse amplitude at the end of strip is larger than at the center because the voltage pulse is reflected at the junction between MCP strip and the circuit board where there is a slight impedance mismatch.
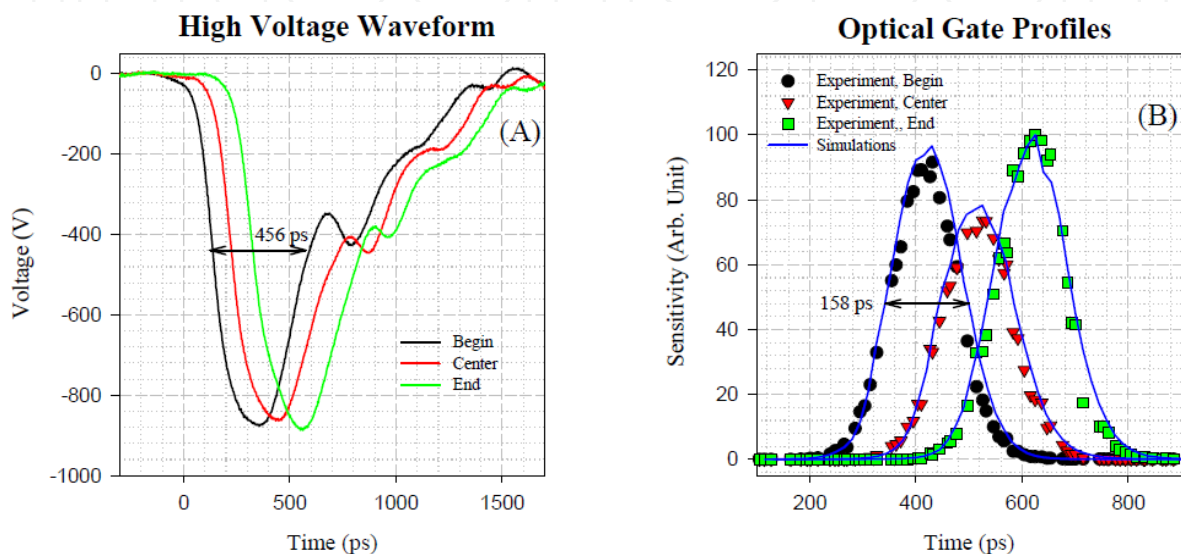
Fig. 8. (A) Measured waveforms at different positions on the strip; (B) measured and simulated gate profiles at various positions along the strip.

The waveforms in Fig. 8(A), used as input for the Monte Carlo model, allowed us to simulate the position-dependent gate profiles by beginning electron cascades at different times during the voltage pulses. In effect, this simulates the different time delays between the short-pulse laser and the HV pulse so that a valid comparison can be made between the simulated and measured profiles. Fig. 8(B) shows such a comparison. The agreement between the measured and simulated gate profiles is excellent. Also notable is that the FWHM of the gate profiles along the entire MCP are within the experimental error of ±10 ps, so the gate profile width is essentially position independent, which is important for HEDP diagnostics applications. There is, however, an obvious change in the gate profile peak, with the peak at the center of the strip about 20–25% smaller than at either end of the strip; this results from voltage pulse attenuation along the strip.

Detector flat-field characterization in pulsed mode provides an interesting comparison between the simulations and experimental measurements. Generally, MCP detector flat-field characterization in pulsed mode is done using a long-pulse x-ray source or UV laser, with the source pulse lasting much longer than the voltage pulse duration. It is also possible to obtain the flat-field of the MCP detector from a short-pulse UV laser by integrating the position-dependent gate profiles. In Fig. 9 sensitivity uniformity along the MCP strip between experimental results and simulations are compared. The integrated intensity of the experimental data here is simply a sum of the position-dependent gate profiles, normalized

for the entire MCP strip. The integrated intensity obtained from the simulations is scaled to the experimental data at 33 mm. The differences between experimental and simulation data are within their error bars. The experimental error bar is a standard deviation within each spatial location of interest, while the error bars on the simulations are taken to be 10%.
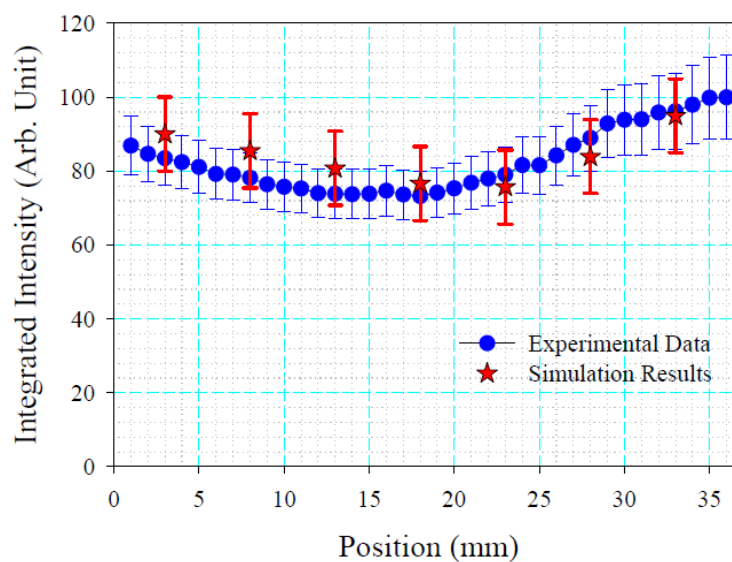

Fig. 9. Simulated and measured detection uniformity along the MCP strip.

7. MCP gain in pulsed mode

To make a comparison to the square wave results shown previously and to the results of Landen et al. (1993), experiments were also conducted to examine how the MCP gain sensitivity varied with peak applied voltage. The voltage pulse from our CPS3 unit with a 150 ps flat-top PFN plus various DC offsets were used to bias the MCP. The delay timing was set so that the laser and HV pulses overlapped at strip's center. Due to the timing jitter, however, the maximum signal was often not at the center of the strip. Although five images were taken, timing jitter was the primary source of error.

For comparison with the experimental results, we ran simulations using the voltage profile shown in Fig. 8(A) for the center of the strip. The electric field due to this voltage pulse was added to the electric field from the measured DC offsets, and electron cascades were launched at the appropriate times to achieve the maximum gain for that particular voltage pulse. An average of five electrons was used to initiate the cascades. To account for uncertainties in the true voltage value on the plate, we incorporated a ±5% uncertainty in the peak voltage pulse value. The results are shown in Fig. 10 along with the experimental data. The error bars on the simulation data points are calculated based on the assumed ±5% uncertainty in the peak of the voltage pulse and a one-sigma uncertainty calculated from the simulated gain distribution. From Fig. 6(A), it seems that the variation of peak voltages along the MCP strip is less than ±5% and so the errors estimated for the simulation are likely an upper limit. Power dependences of 16.9 and 15.4 were observed for the experiments and simulations, respectively. The agreement between results is within the error bars. The higher order power dependence of the relative gain on peak voltage when the flat top of the HV waveform is less than the transit time of cascading electrons in MCP is thus evident.
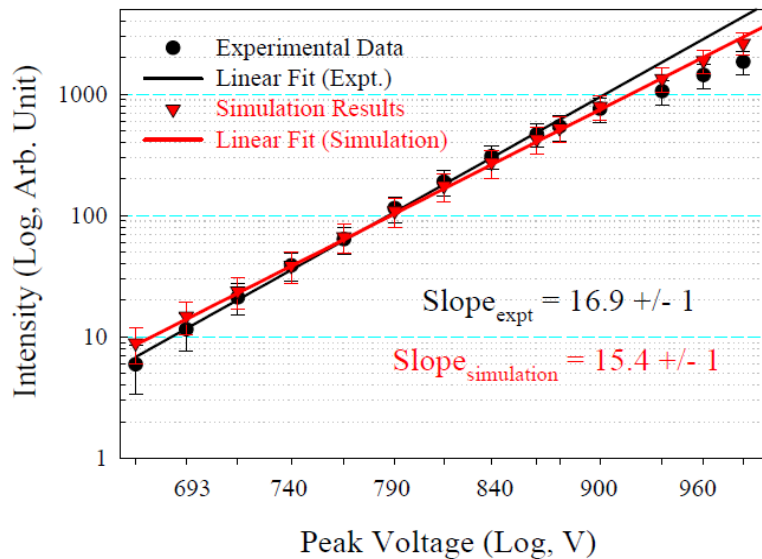
Fig. 10. Simulated and measured relative sensitivity vs. peak voltage.

8. Gain saturation in DC and pulsed modes

It is essential to understand the saturation limit when considering experimental application of MCP detectors. In this section, to examine saturation behavior of MCPs under both DC and pulsed modes, the average intensity of the MCP was calculated over entire MCP strips at each laser flux, while the experimental errors were estimated by the standard deviation of the sensitivity. In the pulsed mode, the delay timing allowed the laser and HV pulses to overlap at the center of the MCP strip. Due to the timing jitter, the maximum signal was often not at the center of the strip; the average peak intensity was a mean value of five maximum intensities over the strips in each selected laser flux, which were also normalized with fluctuation of the laser power. The experimental errors were standard deviations of intensity with the bin size (1 mm) and five laser shots.

In the simulations, the effect of increasing the laser power was approximated by increasing the mean number of primary electrons. A true comparison to the experimental data would require knowledge of the quantum efficiency of the MCP for the 200 nm photons produced by the laser, which is not available in literature. However, given the large number of photons/channel per laser pulse for even the lower fluxes we conclude that it must be about ≤0.1% for the MCP to see no indication of saturation at these fluxes. The comparison of simulations to data is based on the relative increase in primary electron number, assuming that the mean number of primary electrons scales linearly with the laser flux. Thus, we performed simulations with the mean number of primary electrons δ_0 varying between 100 and 5000 for DC bias voltages between –400 and –900 V at 50 V steps. Also, to investigate the detector dynamic range in pulsed mode, we performed simulations using a pulsed waveform measured by the Picoprobe, and with the number of primary electrons, δ_0, varying between 1 and 3000.

DC mode experimental data and simulation results have been plotted together in Fig. 11. The experimental data show appreciable saturation at -700 VDC for photon fluxes >500 nJ/cm² , but saturation at lower fluxes is absent. It is also true that the gain versus voltage sensitivity changes somewhat with laser power. As the laser flux is increased, the gain

becomes slightly less dependent on voltage, changing from about a $G \propto V^{11}$ dependence to more nearly a $G \propto V^9$ dependence before the onset of saturation. The simulations exhibit a similar trend, changing from $G \propto V^{11}$ at a mean of one primary electron to $G \propto V^{8.5}$ in the linear (unsaturated) range at a mean of 5000 primary electrons. This effect, which was first reported in Kruschwitz et al. (2008), implies that this decrease in the gain sensitivity may arise from a "weak" saturation resulting from high electron numbers present in the channel at a given time, even though the MCP gain may not be very high, because the photoelectrons are generated in less than 1 ps by the laser pulse. In other words, the "weak" saturation may be a space charge effect due to a high production rate of photoelectrons.
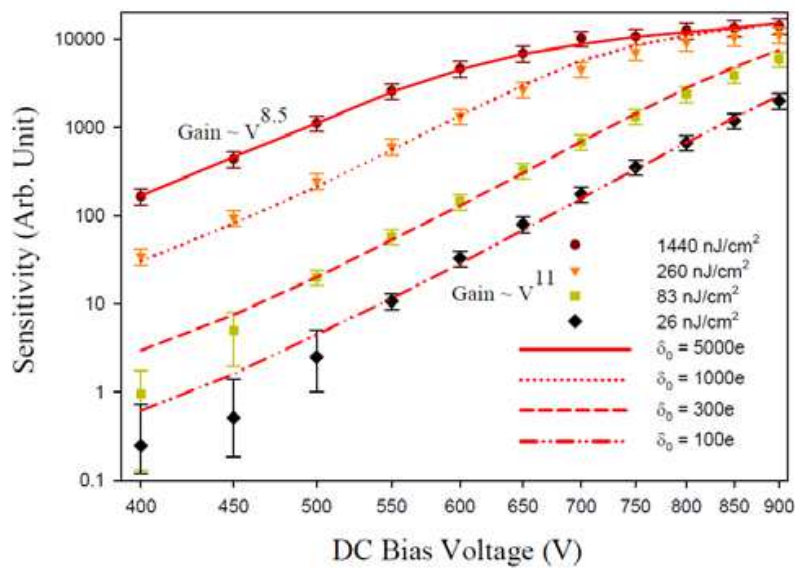
Fig. 11. Simulated and measured MCP sensitivity vs. DC voltage. Data were obtained using a UV laser and neutral density filters to adjust the flux. Simulations were run with different numbers of initial electrons.
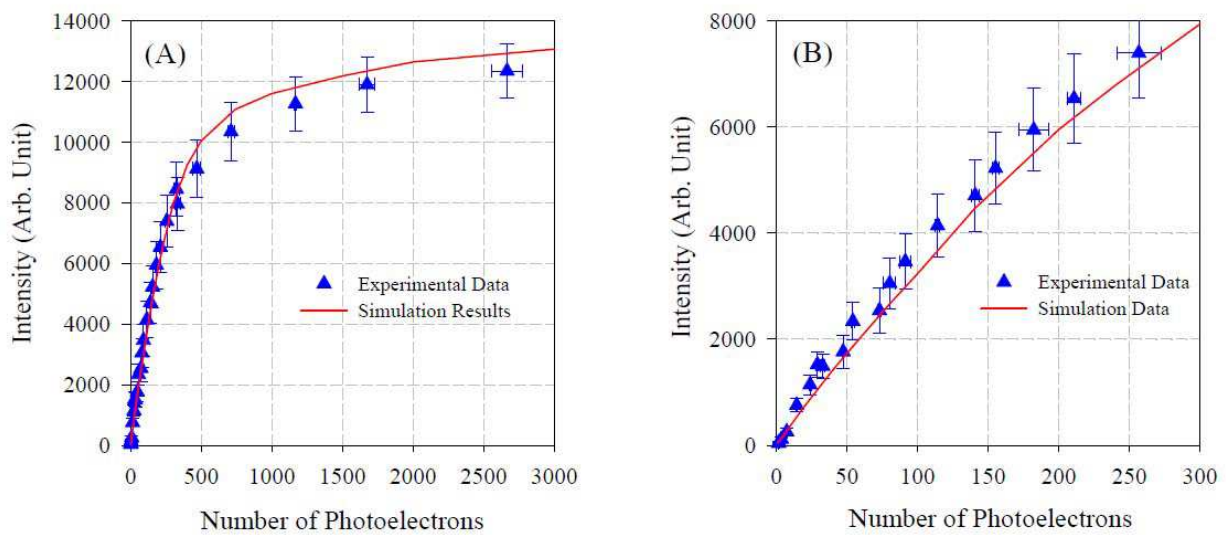
Fig. 12. Simulated and measured MCP saturation behavior in pulsed mode.

Fig. 12 shows a comparison of simulated and measured MCP saturation in pulsed mode. The measured laser flux was converted to a number photoelectrons per pore assuming the MCP's quantum efficiency at 200 nm wavelength is 0.1%, since the absolute detection efficiency of the MCP detector and recording system were not well determined. The number of output electrons was then scaled to the measured output signal. Fig 12(A) shows good agreement for entire range from 1 to 3000 input photoelectrons. A low photon flux range is expanded in Fig. 12(B). The differences between the experimental data and simulation results are well within the experimental error bars. But the simulation results seem in general to be a bit lower in the lower flux range and somewhat higher in the saturation region. It is also interesting that, according to simulations, the saturation limit is about 300,000 electrons per pore, and the onset of nonlinearity is near 100,000 electrons per pore for a 10 μm pore diameter, L/D = 46 MCP. When the MCP gain is set at 100 and assuming a detection limit of 10 electrons, the dynamic range of the MCP could be on the order of just a few hundred.

9. Spatial resolution

A useful characteristic of the three-dimensional electron transport model is that it allows us to predict MCP resolution. Resolution calculations were based on the set of parameters for the MCP camera back imaging system described in the experiments. As described above, the electron position distribution is obtained by calculating the ballistic trajectory of the MCP output electrons hitting the phosphor plate held at a fixed positive potential. The electron scattering from the phosphor surface does not include in the simulation model. The phosphor is located 0.75 mm. from the MCP exit face, which is at ground potential. Experimental measurements of the detector spatial resolution were made using a knife-edge resolution target. For some simulations, we assumed that the conductive gold coating extended into the channel output a distance of about 1.5 channel diameters, or 15 μm. This end spoiling created an electron focusing effect, which has been detailed previously (Eberhardt, 1979; Bronshteyn et al., 1979; Koshida & Hosobuchi, 1985; Koshida, 1986).
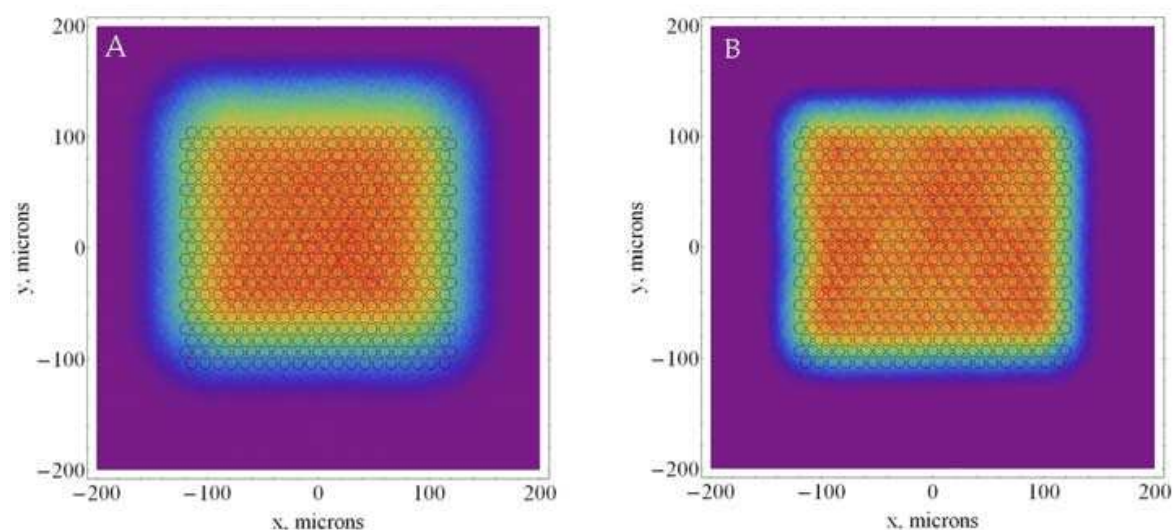

Fig. 13. Simulated output electron distributions on phosphor: (A) V_{ph} = 1000 V; (B) V_{ph} = 4000 V for 10 μm L/D = 46 MCP with a 0.75 mm gap between the MCP and phosphor.
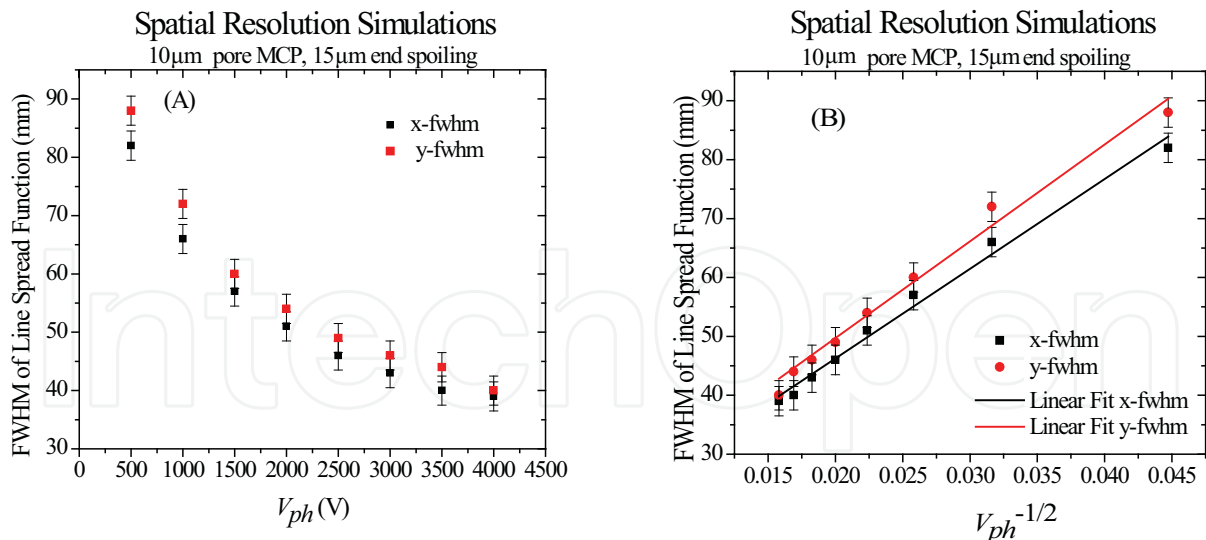
Fig. 14. Spatial resolution vs. applied voltages (A) V_{ph} and (B) $V_{ph}^{1/2}$ on the phosphor with 15 um of end spoiling.
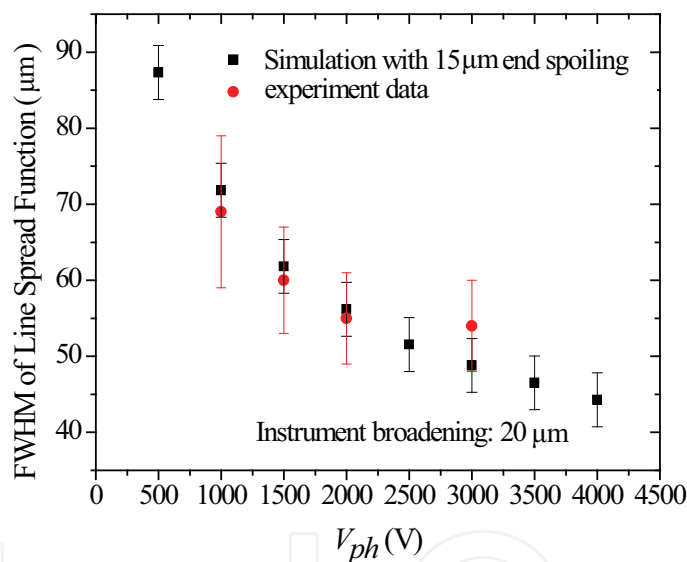

Fig. 15. A comparison between measured and simulated spatial resolution.

For our spatial resolution calculations, we have generated a set of output electrons from a 430-channel array in a hexagonal-packed geometry with a center-to-center distance of 12 μm. Electron cascades were launched in each pore to approximate a two-minute exposure on the Manson x-ray source. An orthogonal x–y coordinate system was established in the phosphor plane with the bias angle along the y axis. Fig. 13 shows a simulated image of the output from the 430-pore array; locations of the pore output ends are shown. 15 μm of pore end spoiling was assumed. The two images are for V_{ph} = 1000 V and V_{ph} = 4000 V. Line spread functions (LSF) were calculated by taking the first derivative of the electron distribution functions, such as those shown in Fig. 13. The FWHMs of the LSFs were calculated for phosphor potentials V_{ph} ranging from 500 to 4000 V. The resolution in the x and y directions, defined as the FWHM of the LSFs, are plotted in Fig. 14. In Fig. 14(A) they are plotted simply as function of V_{ph}, while in Fig. 14(B) they are plotted as a function of V_{ph}^{-}

$^{1/2}$. A simple analytical expression for the spatial resolution δ of an MCP detector indicates that the relationship between δ and V_{ph} is $\delta \propto V_{ph}^{-1/2}$ (Kilkenny, 1991) and, so, a plot such as that in Fig. 14(B), should yield a straight line. From Fig. 14(B), we see that such a relationship does in fact hold, in the x and y directions. It is also evident from Fig. 14 that the LSF FWHM in the y direction is slightly larger than in the x direction.

Fig. 15 compares the experimental measurements of the spatial resolution of the MCP plus CCD detector system and the simulations of the MCP spatial resolution. Experimental measurements and simulations have been performed for V_{ph} between 500 and 4000 V. For the simulated resolutions, 20 μm instrument resolution broadening was added in quadrature to the simulated LSF FWHM with 15 microns of end spoiling, and the x and y FWHM were averaged. The measured and simulated results show an excellent agreement.

10. Simulations of small-pore MCPs

An important aspect of the Monte Carlo model is its adaptability. It is a relatively simple matter to investigate MCPs with a broad range of parameters. Small-pore MCPs, with pore diameters down to 2 μm and a center-to-center spacing of 3 μm, are now available. The Monte Carlo code was used to study such MCPs and their potential characteristics for imaging applications. Potential benefits to using small-pore MCPs would be faster time response, which translates to superior time resolution, and perhaps improved spatial resolution due to the smaller pore size. Drawbacks would be inferior dynamic range and the small sizes of the MCPs (typically ~ 1 cm diameter and thicknesses on the order of 100 μm), which make them far more delicate and difficult to work with than their larger-pored brethren.

In order to understand potential advantages and limitations of the small-pore MCP, we modelled MCPs with an L/D ratio of 60 and an 8-degree bias angle for 10 and 2 μm pore sizes. Cascades were started with a mean of three electrons. Fig. 16(A) and (B) shows the simulated DC sensitivity versus voltage for L/D = 60, D = 10 μm pore MCP, and D = 2 μm pore MCPs respectively. The gain curves look quite similar, as one would expect given that the L/D ratio is identical for both MCPs. The 2 μm pore MCP begins to show some nonlinearity at slightly less than 10^4 electrons versus slightly less than 10^5 for the 10 μm pore MCP. Due to the decrease in effective inner surface area between the 2 and 10 μm pores, the saturation limit of the 2 um pore MCP can be reduced by more than a factor of ten if surface charge depletion is the dominant factor. The small-pore MCP's dynamic range can thus be expected to be reduced by about a factor of ten or more compared to the 10 μm pore MCP. Fig. 16(C) and (D) show the transit time distributions for the same MCPs. As shown, the 2 μm pore MCP has a much shorter transit time (55–60 ps) and a much narrower TTS than the 10 μm pore MCP. As shown in Section 9, this implies that one could design an imager with temporal resolution near 50 ps without sacrificing much gain, something much desired in the HEDP community. An attempt to achieve gate times in the 30 – 40 ps range was reported by Bradley et al (1995) using an L/D = 20, D = 10 μm pore MCP available at the time. A -1500 V pulse was applied to that MCP in their calculated estimate of the gate time. That voltage might not be physically possible due to potential arcing through the 220 μm MCP. Our simulation here using L/D = 80 2 μm pore MCP implies that an x-ray imager with an optical gate near 50 ps can potentially be realized with currently available technology (i.e., MCPs and HV pulsers).
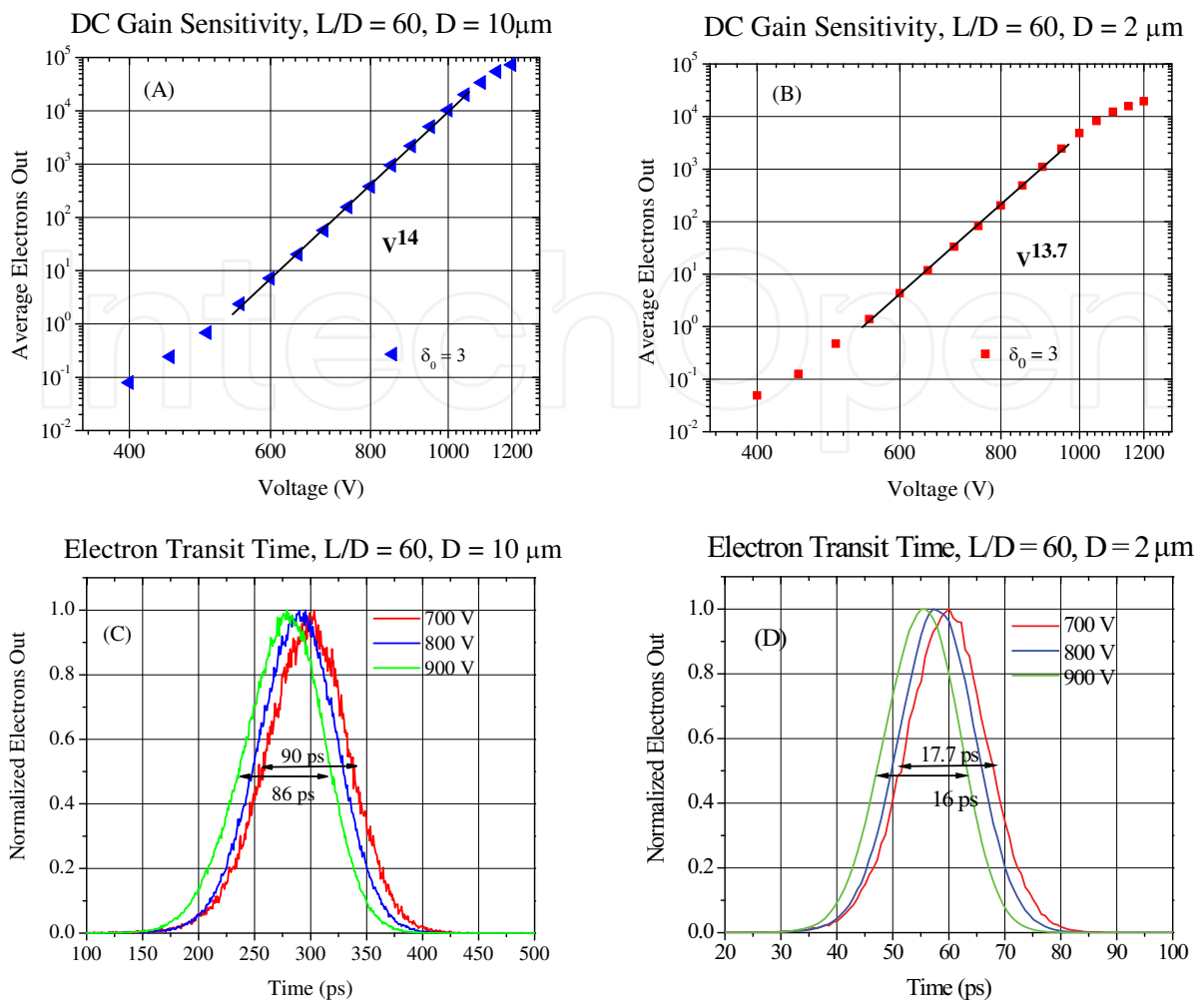
Fig. 16. A comparison of DC sensitivity (A&B) and transit time and TTS (C&D)between 10 and 2 µm L/D ratio of 60 MCPs by the simulations.

Simulations of the gate profiles for the 2 µm pore MCPs were also performed using the same setup described earlier for the L/D = 46, D = 10 µm MCPs: we used a measured voltage pulse from a Kentech CPS3 pulser with a 300 ps flat-top PFN, and cut 50 ps portions from the flat region, as shown in Figure 5(A). MCPs with L/D = 46, 60, and 80 were investigated. Simulated gate profiles of these MCPs are shown in Figs. 17(A), (B), and (C) separately. Gate profiles for the shortest voltage pulses are about 55 ps, suggesting the possibility of achieving imaging time resolutions of near 50 ps using readily available technology. Such resolutions are of great interest in the HEDP community. Fig. 17(D) shows relative sensitivity variations in both peak height and integrated area. Because 2 µm MCPs have a shorter transit time, there is not much change in peak height when the flat top is longer than 10 ps. When the optical gate is near 55 ps, the peak height is reduced less than a factor of five. Therefore, if a pulse with a faster rising and falling edge could be achieved, then even shorter time resolutions may be possible.

Our study of small-pore MCPs is completed by investigating the spatial resolution of a hypothetical imaging system using a 2 µm pore MCP. Like the 10 µm pore MCP spatial resolutions simulations, a grouping of 430 pores was studied. A d = 0.5 mm gap between the output face of the MCP and the phosphor was used in most of the simulations, but a few were done with a gap of d = 0.25 mm. One hundred cascades were started in each pore in

the cluster and the output electrons were accelerated by the MCP–phosphor bias voltage, V_{ph}. Values of V_{ph} ranging from 500 to 4000 V were investigated for those simulations using d = 0.5 mm, while V_{ph} values of 500 to 2000 V were used for those simulations using d = 0.25 mm. Fig. 18 shows the simulated electron output for the 430-pore cluster for V_{ph} = 1000 V and V_{ph} = 4000 V, d = 0.5 mm with 3 µm (1.5 channel diameters) end spoiling. The output electron distribution is clearly far more diffuse for the V_{ph} = 1000 V simulations. Fig. 19 shows the FWHM of the LSFs for all of the investigated values of V_{ph}, plotted both as a function of V_{ph} and as a function of $V_{ph}^{-1/2}$.

There appears to be a linear relationship in both the x- and y-directions between the FWHM of the LSF and $V_{ph}^{-1/2}$, at least for voltages greater than 2000 V. Similar to the 10 µm pore MCP simulations, the FWHM in the x-direction is smaller than in the y-direction for V_{ph} ≥2000 V. In contrast to those results, however, for V_{ph} <2000 V the FWHM in the y-direction is much smaller than in the x-direction. In fact, the FWHM in the y-direction appears to be independent of V_{ph} for V_{ph} <2000 V. For both sets of small-pore simulations the spatial resolution can be expected to be improved relative to the 10 µm pore MCP. The FWHM of the simulated LSFs are smaller by ~10 µm for the 2 µm pore MCPs.
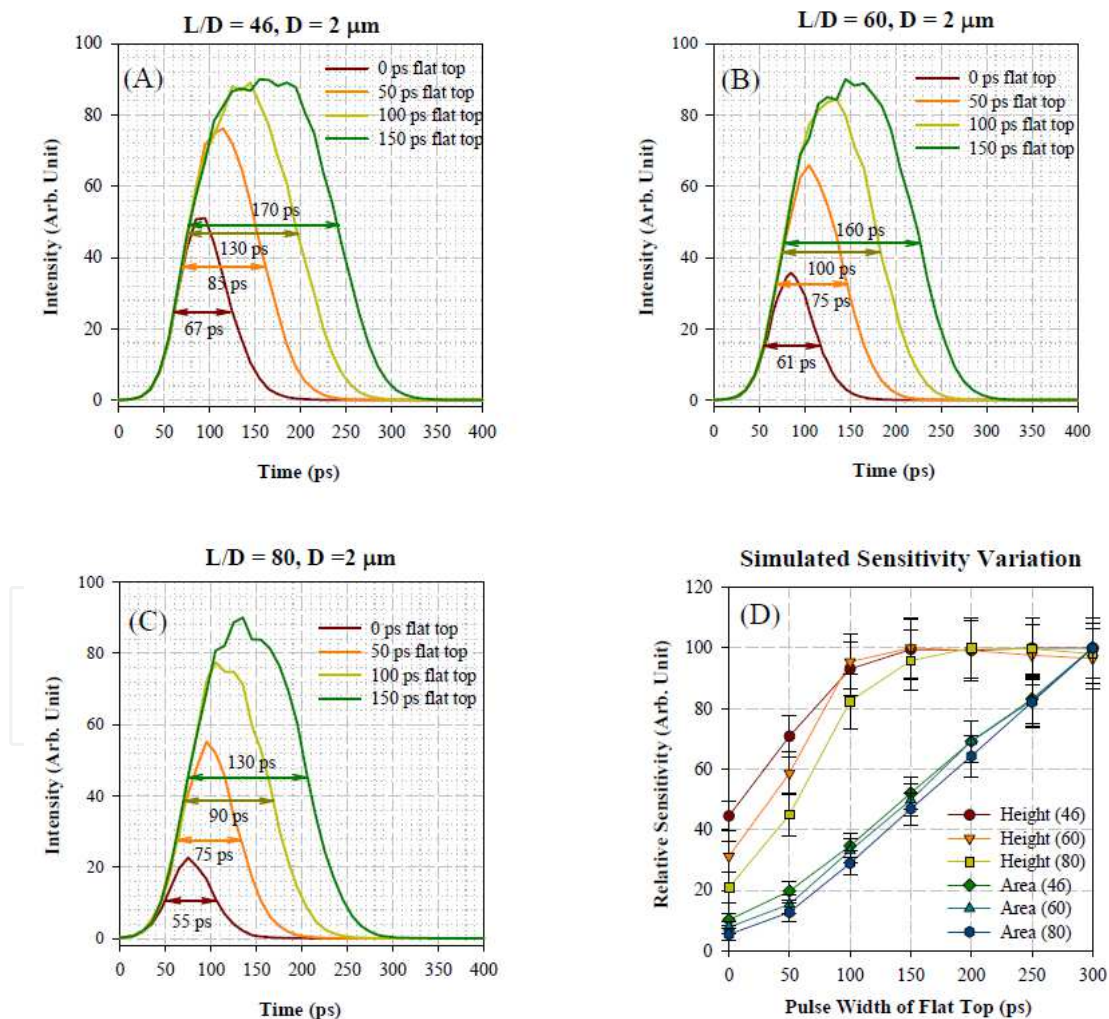
Fig. 17. Simulated optical gate profiles of 2 µm L/D = 46, 60, and 80 MCPs in (A), (B), and (C) using input voltage waveforms in Fig. 5(A); relative detection sensitivity in both peak height and integrated area for these MCPs are shown in (D).
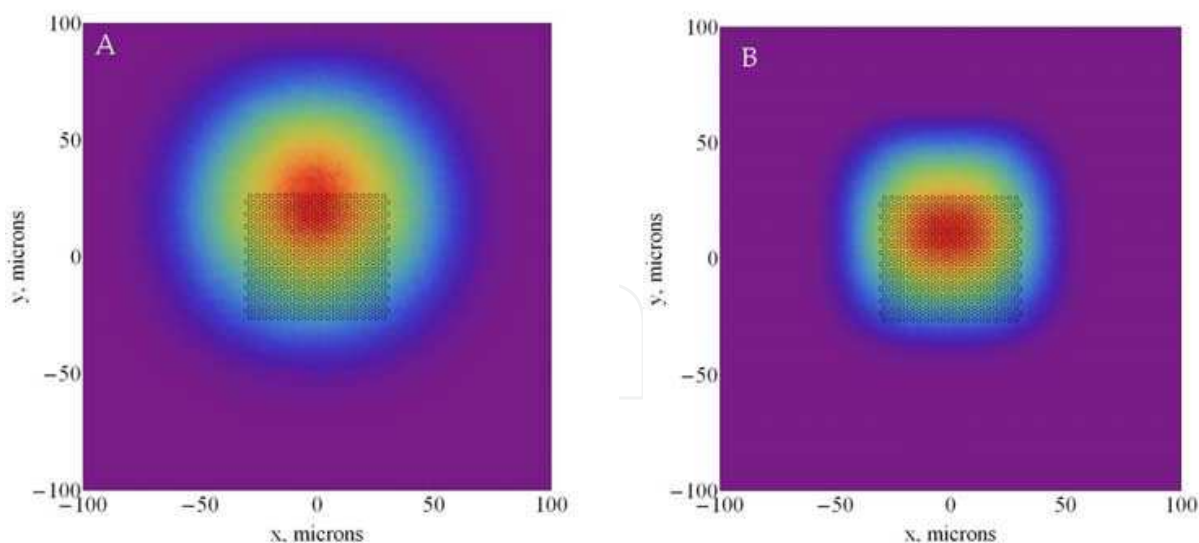
Fig. 18. Simulated output electron distributions on phosphor: (A) V_{ph} = 1000 V; (B) V_{ph} = 4000 V for 2 μm L/D = 46 MCP with a 0.50 mm gap between the MCP and phosphor.
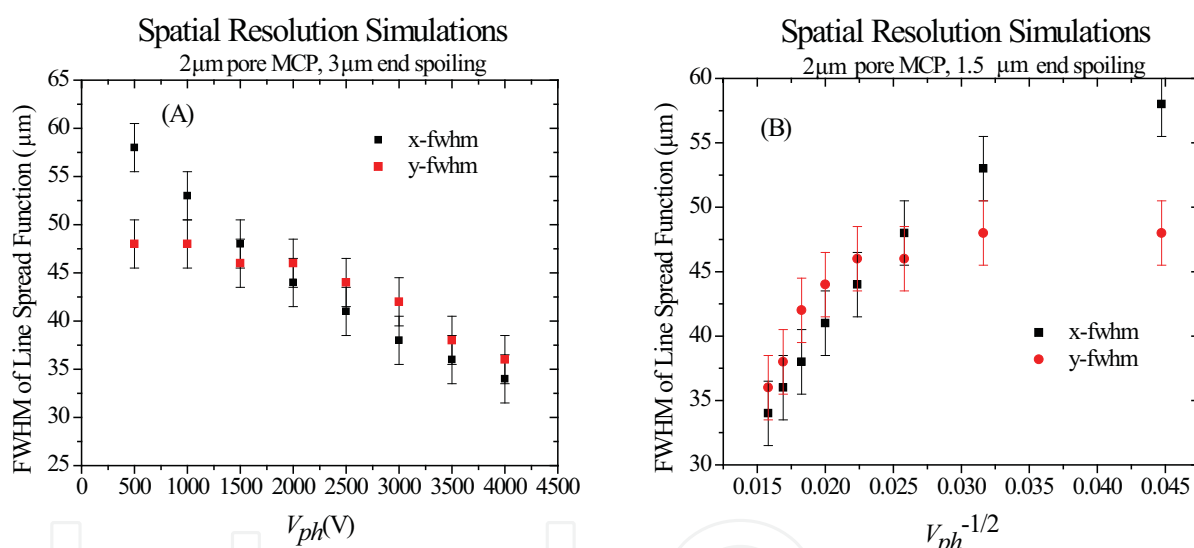

Fig. 19. Simulated spatial resolutions of 2 μm L/D = 46 MCP with 3 μm (1.5 channel diameters) of end spoiling in parallel (x) and perpendicular (y) directions with bias angle of the pore and with a 0.50 mm gap between the MCP and phosphor(A) V_{ph} and (B) $V_{ph}^{1/2}$.

For the proximity focused approximation, one would expect the spatial resolution to increase linearly when the gap, d, between the MCP output and the phosphor is reduced (Kilkenny, 1991). For our final set of 2 μm pore MCP spatial resolution studies, the phosphor was placed closer to the MCP output, such that d = 0.25 mm. This is indeed rather close and may not be physically achievable without arcing. However, the fact that the small-pore MCPs are usually rather small may make this MCP–phosphor distance obtainable. The results show that the LSF FWHM at V_{ph} = 2000 V is near 30 μm, smaller than in the d = 0.5 mm cases. This is a change of about 15 microns, somewhat less than the expected factor of two from the proximity focused approximation. The dependence versus $V_{ph}^{-1/2}$ appears to be linear across the entire simulated range of V_{ph} in the x-direction, however.

In conclusion, it appears that small-pore MCPs may offer some significant improvements over 10 μm pore MCPs for fast-gated imaging applications. In particular, much higher time resolutions may be achievable, with optical gate widths near 50 ps a possibility. Modest improvements on the order of 10 μm in spatial resolution (measured as FWHM of the LSF) may also be achievable.

11. Conclusion

We have discussed our Monte Carlo simulation model, developed as a tool for assisting with the design of high-speed, time-gated x-ray cameras and for interpreting their data. The code uses a fairly standard set of equations for determining secondary emission yields, based in part on experimental data obtained with MCP lead glass. It also takes into account elastic reflections of low-energy electrons from the channel wall and requires that the total secondary electron energy not exceed the energy of the parent primary electron.

The plentiful experimental data we have for 0.46 mm thick, 10 μm pore diameter MCPs allowed us to test our simulation code and fine-tune imprecisely known MCP secondary emission parameters. With this fine-tuning, our simulations of gain vs. DC bias voltage and of MCP spatial resolution achieve excellent agreement with experimental data.

In addition we studied the behavior of the electron cascade in an MCP under a time-dependent voltage pulse. We focused in particular on voltage pulses of duration shorter than or comparable to the DC electron transit time in an MCP. Simulations using ideal square waves of varying widths and with varying DC offsets illustrate some interesting behavior of MCPs in pulsed mode. In particular, we observe an increase in the MCP relative sensitivity (i.e., the MCP gain exponent) with peak voltage for pulse widths shorter than the transit time. However, this increase in the relative sensitivity is accompanied by a marked decrease in absolute sensitivity (the actual MCP gain). We see similar behavior in simulations using voltage pulses measured on MCP striplines. These latter simulations agree with experimental data obtained using a short-pulse UV laser.

Simulated and measured optical gate profiles for a gated x-ray camera with a 150 ps quasi-flat-top voltage pulse were presented. Voltage waveforms were measured at positions along an MCP stripline using a high-impedance, high-bandwidth probe. These waveforms were used in Monte Carlo code to calculate position-dependent gate profiles. Comparisons with gate profiles measured experimentally using a short-pulse UV laser demonstrated excellent agreement, both for the gate profile widths and the peak relative sensitivities.

We have also shown results of a simulation study of the potential performance of 2 μm pore MCPs for fast-gated imaging applications. Results of 2 μm pore MCP simulations were compared with simulated (and some measured) results from a 10 μm pore MCP. We found that for the 2 μm pore MCPs, gate profiles near 50 ps are potentially achievable with technology readily available. Additionally, we found that the simulated spatial resolutions are somewhat superior to what is achievable with a 10 μm pore MCP. Thus, small-pore MCPs present an intriguing possibility for future HEDP imaging diagnostics.

12. Acknowledgments

13. References

Authinarayanan, A. & Dudding, R. (1976). Changes in secondary electron yield from reduced lead glasses. *Adv. Electron Phys. A*, 40, 167-181

Bailey, J. E., Chander, G., Slutz, S., Golovkin, I., Lake, P., MacFarlane, R., Mancini, T., Burris-Mog, T., Cooper, G., Leeper, R., Mehlhorn, T., Moore, T., Nash, T., Nielsen, D., Ruiz, C., Schroen, D., & Varnum, W. (2004). Hot dense capsule-implosion cores produced by Z-pinch dynamic hohlraum radiation. *Phys. Rev. Lett.*, 92, 085002-1 -4

Bradley, D. K., Bell, P.M., Landen, O.L., Kilkenny, J.D., & Oertel, J. (1995). Development and characterization of a pair of 30 -40 ps x-ray framing cameras. Rev. Sci. Instrum. 66, 717-718

Bruining, H. (1954). *Physics and Applications of Secondary Electron Emission*, Pergamon, 0080090141, London

Bronshteyn, I., Yevdokimov, A., Stozharov, V., & Tyutikov, A. (1979). Differential secondary-emission characteristics of microchannel plates. *Radio Eng. Electron. Phys.*, 24, 150 152; 871-874

Choi, Y. & Kim, J. (2000). Monte Carlo simulations for tilted-channel electron multipliers. *IEEE Trans. Elec. Dev.*, 47, 1293–1296

Cimino, R., Collins, I., Furman, M., Pivi, M., Ruggiero, F., Rumolo, G., & Zimmerman, F. (2004*).* Can low energy electrons affect high energy physics accelerators? *Phys. Rev. Lett.*, 93, 014801-1 -4

Eberhardt, P. (1979). Gain model for microchannel plates. *Appl. Opt.*, 18, 1418-1423

Fraser, G., Barstow, M., Whiteley, M., & Wells, A. (1982). Enhanced soft x-ray detection efficiencies for imaging microchannel plate detectors. *Nature (London)*, 300, 509-511

Fraser, G., Barstow, M., Pearson, J., Whiteley, M., & Lewis, M. (1984). The soft x-ray detection efficiency of coated microchannel plates. *Nucl. Instrum. Methods*, 224, 272 -286

Gatti, E., Oba, K., & Rehak, P. (1983). Study of the electric field inside microchannel plate multipliers. *IEEE Trans. Nucl. Sci.*, NS-30, 461–468

Guest, A. (1971). A computer model of channel multiplier plate performance. *Acta Electronica*, 14, 79-97

Hirata, M., Cho, T., Takahashi, E., Yamaguchi, N., Kondoh, T., Matsuda, K., Aoki, S., Tanaka, K., Maezawa, H., & Miyoshi, S. (1992). X-ray detection characteristics of gold photocathodes and microchannel plates using synchrotron radiation (10 eV– 82.5 keV). *Nucl. Instrum. Methods Phys. Res. B*, 66, 479–484

Ito, M., Kume, H., & Oba, K. (1984). Computer analysis of the timing properties in micro channel plate photomultiplier tubes. *IEEE Trans. Nucl. Sci.*, NS-31, 408–412

Kilkenny, J. (1991). High speed proximity focused X-ray cameras. *Laser and Particle Beams, 9*, 49–69

Koshida, N. & Hosobuchi, M. (1985). Energy distribution of output electrons from a microchannel plate. *Rev. Sci. Instrum.*, 56, 1329–1331

Koshida, N. (1986). Effects of electrode structure on output electron energy distribution of microchannel plates. *Rev. Sci. Instrum.*, 57, 354-358

Kruschwitz, C. A., Wu, M., Moy, K., & Rochau, G. (2008). Monte Carlo simulations of high-speed, time-gated microchannel-plate based x-ray detectors: saturation effects in DC and pulsed modes and detector dynamic range. *Rev. Sci. Instrum.*, 79, 10E911-1 -4

Landen, O., Bell, P., Oertel, J., Satariano, J., & Bradley, D. (1994). Gain uniformity, saturation and depletion in gated microchannel-plate x-ray framing cameras. *Proc. SPIE,* 2002, 2-13

Landen, O., Abare, A., Hammel, B., Bell, P., & Bradley, D. (1993). Detailed measurements and shaping of gate profiles for microchannel-plate-based framing camera. *Proc. SPIE,* 2273, 245-254

Landen, O., Lobban, A., Tutt, T., Bell, P., Costa, R., Hargrove, D., & Ze, F. (2001). Angular sensitivity of gated microchannel plate framing cameras. *Rev. Sci. Instrum.*, 72, 709 -

McCarville, T., Fulkerson, S., Booth, R., Emig, J., Young, B., Anderson, S., & Heeter, B. (2005). Gated x-ray intensifer for large format simultaneous imanging. *Rev. Sci. Instrum.* 76, 103501-1 -6

Melamid, A., Khachatryan, Z., Guzhov, A. (1972). Photoelectric emission in the wavelength region 500–1700 Å. *J. Appl. Spect.,* 16, 262-265

Oertel, J., Aragonez, R., Archuleta, C., Barnes, C., Casper, L., Fatherley, V., Heinrichs, T., King, R., Landers, D., Lopez, F., Sanchez, P., Sandoval, G., Schrank, L., Walsh, P., Bell, P., Brown, M., Costa, R., Holder, J., Montelongo, S., & Pedersen, N. (2006). Gated x-ray detector for the National Ignition Facility. *Rev. Sci. Instrum.*, 77, 10E308-1-4

Pawley, C. J & Deniz, D. V. (2000) Improved measurements of noise and resolution of x-ray framing cameras at 1 -2 keV. *Rev. Sci. Instrum.* 71. 1286-1296

Price, G. & Fraser, G. (2001). Calculation of the output charge cloud from a microchannel plate. *Nucl. Instrum. Methods Phys. Res. A,* 474, 188-196

Robey, H., Bundil, K., & Remington, B. (1997). Spatial resolution of gated x-ray pinhole cameras. *Rev. Sci. Instrum.*, 68, 792 -795

Rochau, G., Bailey, J., Chandler, G., Nash, T., Nielsen, D., Dunham, G., Garcia, O., Joseph, N., Keister, J., Madlener, M., Morgan, D., Moy, K., & Wu, M. (2006). Energy dependent sensitivity of microchannel plate detectors. *Rev. Sci. Instrum.*, 77, 10E323-1-4

Rochau, G., Wu, M., Kruschwitz, C., Joseph, N., Moy, K., Bailey, J., Crain, M., Thomas, R., Nielsen, D., & Tibbitts, A. (2008). Measurement and modeling of pulsed microchannel plate operation. *Rev. Sci. Instrum.,* 79, 10E902-1 - 6

Scholtz, J., Dijkkamp, D., & Schmitz, W. (1996). Secondary electron emission properties. *Philips. J. Res.,* 50, 375-389

Shikhaliev, P. (1997). Hard x-ray detection model for microchannel plate detectors. *Nucl. Instrum. Meth. in Phys. Res. A,* 398, 229-237

Vaughan, J. (1989). A new formula for secondary emission yield. *IEEE Trans. Elec. Devices,* 36, 1963-1967

Wiza, J. (1979). Microchannel plate detectors. *Nucl. Instrum. Methods,* 162, 587 -601

Wu, M., Kruschwitz, C., Morgan, D. , & Morgan, J. (2008). Monte Carlo simulations of MCP detectors. I. Steady-state voltage bias results. *Rev. Sci. Instrum.*, 79, 073104-1 -7

Ze, F., Landen, O., Bell, P., Turner, R., Tutt, T., Alvarez, S., & Costa, R. (1999). Investigation of quantum efficiencies in multilayered photocathodes for microchannel plate applications. *Rev. Sci. Instrum.,* 70, 659-662
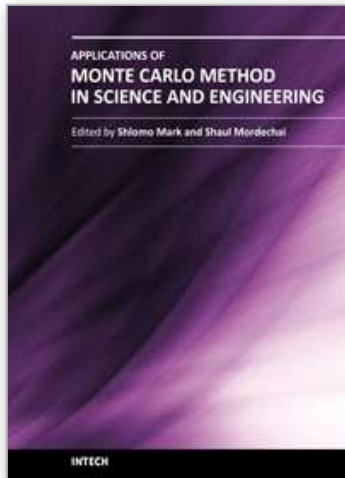
Applications of Monte Carlo Method in Science and Engineering

Edited by Prof. Shaul Mordechai

In this book, Applications of Monte Carlo Method in Science and Engineering, we further expose the broad range of applications of Monte Carlo simulation in the fields of Quantum Physics, Statistical Physics, Reliability, Medical Physics, Polycrystalline Materials, Ising Model, Chemistry, Agriculture, Food Processing, X-ray Imaging, Electron Dynamics in Doped Semiconductors, Metallurgy, Remote Sensing and much more diverse topics. The book chapters included in this volume clearly reflect the current scientific importance of Monte Carlo techniques in various fields of research.

How to reference

In order to correctly reference this scholarly work, feel free to copy and paste the following:

INTECH
open science | open minds